Flight dynamics and stability of a tethered inflatable Kiteplane

E.J. Terink[*], J. Breukels[†], R. Schmehl[‡], and W.J. Ockels[§]
Delft University of Technology, Delft, The Netherlands

The combination of lightweight flexible membrane design and favorable control characteristics renders tethered inflatable airplanes an attractive option for high-altitude wind power systems. This paper presents an analysis of the flight dynamics and stability of such a Kiteplane operated on a single-line tether with a two-line bridle. The equations of motion of the rigid body model are derived by Lagrange's equation, which implicitly accounts for the kinematic constraints due to the bridle. The tether and bridle are approximated by straight line elements. The aerodynamic force distribution is represented by 4 discrete force vectors according to the major structural elements of the Kiteplane. A case study comprising analytical analysis and numerical simulation reveals, that for the specific kite design investigated, the amount and distribution of lateral aerodynamic surface area is decisive for flight dynamic stability. Depending on the combination of wing dihedral angle and vertical tail plane size, the pendulum motion shows either diverging oscillation, stable oscillation, converging oscillation, aperiodic convergence, or aperiodic divergence. It is concluded that dynamical stability requires a small vertical tail plane and a large dihedral angle to allow for sufficient sideslip and a strong sideslip response.

---

[*] Researcher, ASSET Institute, Kluyverweg 1, 2629HS, Delft, The Netherlands.
[†] Ph.D. Candidate, ASSET Institute, Kluyverweg 1, 2629HS, Delft, The Netherlands.
[‡] Associate Professor, ASSET Institute, Kluyverweg 1, 2629HS, Delft, The Netherlands.
[§] Professor, chair holder, and director of ASSET, ASSET Institute, Kluyverweg 1, 2629HS, Delft, The Netherlands.

NOMENCLATURE

A = aspect ratio

$\overline{c}$ = mean aerodynamic cord, m

C_D = aerodynamic drag coefficient

C_L = aerodynamic lift coefficient

$C_{m_{ac}}$ = pitch moment coefficient

C_X = aerodynamic force coefficient in X

C_Y = aerodynamic force coefficient in Y

D = aerodynamic drag, N

d = tether damping constant, Ns/m

e = Oswald factor

$\mathbf{F}_a$ = aerodynamic force vector, N

F_B = bridle force, N

$\mathbf{F}_{GS}$ = ground station force, N

F_Z = gravitational force, N

$\mathbf{g}$ = gravitational acceleration vector, m/s^2

$\mathbb{I}$ = inertia matrix, kgm^2

i = angle of incidence, deg

k = tether spring constant, N/m

L = aerodynamic lift, N

l = length, m

$\mathbf{M}_a$ = aerodynamic moment vector, Nm

m_g = kite mass excluding confined air, kg

m_k = kite mass, kg

$M_{w_{ac}}$ = wing pitching moment, Nm

Q = generalized force, N

q = genralized generalized coordinate

$\mathbf{r}$ = position vector, m

S = surface area, m^2

T = kinetic energy, J

$\mathbb{T}_{BA}$ = transformation matrix for frame A to B

V = potential energy, J

v = velocity, m/s

$\mathbf{v}$ = velocity vector, m/s

X = aerodynamic force in X direction, N

X, Y, Z = Cartesian axis system

x, y, z = Cartesian coordinates, m

Y = aerodynamic force in Y direction, N

$\overline{y}$ = spanwise MAC location, m

y_b = bridle separation, m

α = angle of attack, deg

β = sideslip angle, deg

Γ = dihedral angle, deg

δ = bridle geometry angle, deg

ϵ = downwash angle, deg

θ = pitch angle, deg

θ_T = pendulum mode angle, deg

Λ = sweep angle, deg

λ = wing taper ratio

ζ = aerodynamic element orientation angle, deg

ρ = air density, kg/m^3

ϕ = zenith angle, deg

χ = bridle angle, deg

ψ = azimuth angle, deg

$\boldsymbol{\omega}$ = angular velocity vector, rad/s

Subscripts

ac = aerodynamic center

app = apparent

cg = center of gravity

f = vertical tail fin

HT = horizontal tail

l = local

LE = leading edge

lw = left wing

rw = right wing

T = tether

t = tail

VT = vertical tail

W = wind

w = wing

Superscripts

a = aerodynamic reference frame

B = body reference frame

E = Earth reference frame

T = tether reference frame

I. Introduction

KITES are among the earliest man-made flying objects in history and have been used for a wide variety of purposes [1]. Especially from 1860 to 1910, kites emerged as an important technology for scientific and technical applications such as in meteorology, aeronautics, wireless communication and aerial photography. Although the airplane has subsequently taken over these application areas, kites have made a comeback as major recreational device devices. The increasing shift toward sustainable energy generation and propulsion has triggered a renewed interest in kites for industrial applications, a major driver being the potential of the technology to efficiently exploit the abundant wind at higher altitudes [2, 3]. Using kites for power generation has first been proposed and systematically analyzed by Loyd in 1980 [4], however, subsequent research and development activities were low before the presentation of the 'Laddermill' concept, by Ockels in 1996 [5, 6]. Since then, the number of institutions actively involved in kite power has increased rapidly, with several multi-million dollar projects [7–9].

Various concepts and ideas have been proposed to exploit the wind currents at higher altitudes [10, 11]. One of the concepts is the pumping kite concept [12, 13], where the tether, pulled by lifting bodies, drives a drum that is connected to a generator to produce electricity. By alternating between a high power producing upstroke and a low power consuming downstroke, net energy is generated. The main advantages of such a system over conventional wind turbines are the higher operational flexibility and the ability to exploit the stronger and steadier wind at higher altitudes. However, the high degree of freedom in the design and operation of kite power systems also leads to control challenges. Compared to an airplane, the flight dynamics of a kite are constrained by the tether and bridle system. However, this does not mean that kites are more stable and easier to control. Research indicates that the presence of a tether may raise stability issues [14–16].

A successful pumping kite power system requires a kite that is not only agile and aerodynamically efficient to maximize the power output, but also stable to minimize the control effort. In addition, a low lift mode - in kite terminology called depower - is necessary to implement a swift low power consuming downstroke. Some kite types are naturally stable on a single-line, such as box kites, sled kites, delta kites and some ram-air kites, but neither meets the full set of requirements. The Kiteplane developed at the ASSET chair of Delft University of Technology and displayed in Fig. 1, is specifically designed to operate in a pumping kite concept [17–19]. The Kiteplane is an airplane shaped kite constructed with inflatable beams and canopy surfaces. It features a bridled wing, efficient aerodynamics for a kite, and easy angle of attack control. However, flight tests have indicated that the prototype of 2009 suffers from a pendulum instability, which is an unstable oscillation in the crosswind plane.

This paper presents a rigid body model of a single-line bridled Kiteplane to investigate the

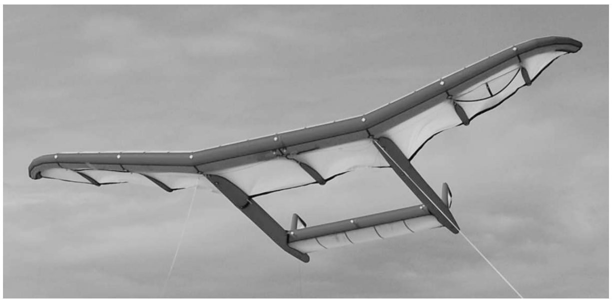

Fig. 1: The Kiteplane.

influence of geometry on flight dynamics and stability. The bridle is used as a structural element to alleviate the wing bending moment, but it also constrains the rotational freedom of the kite. The roll and yaw motion of the kite are coupled, because the bridle acts as a revolute joint between the tether and the Kiteplane. At a high elevation angle, the roll motion is constrained, and at a low elevation angle, the yaw motion. At intermediate angles, the motion is a combination of roll and yaw. The continuous aerodynamic load distribution is represented by discrete forces and moments acting on the aerodynamically active structural elements of the Kiteplane to make the model largely parametric in geometry. The kite system model is described in the methodology section and applies to kites that are build out of straight aerodynamic elements, and which global geometry and inertia can be assumed constant.

The developed model is subsequently employed to analyze the stability of the Kiteplane in a case study. Both analytical and numerical results are obtained and compared qualitatively to each other and a flight test. Stable and unstable domains are identified and tested on robustness by varying geometry and operational conditions in the simulations.

II. Methodology

This paper focuses on the influence of geometrical design parameters on the global dynamics of a single-line kite system. Several modeling methods are found in Williams et al. [20]. Optimal control problems for kite systems are often solved using point-mass models [21–23]. Kite performance is investigated using lumped mass and massless models [24]. For stability, however, attitude dynamics are essential and a point-mass model cannot be used. Also, a flexible body model would not provide pure geometry-stability relations. Given this scope and the philosophy that the best model is the smallest model that describes the behavior of interest, a rigid body approach is selected to model the kite.

Moreover, to investigate the impact of geometry changes on stability, a parametric approach is required for the aerodynamic forces. To this end, an aerodynamic element discretization is developed similar to Meijaard et al. [25].

The equations of motion are derived using Lagrange's equation of the second kind [26], a method used frequently for the constrained kite systems [27–29].

A. Kite system definition

The kite system consists of a ground station, a tether and a kite. The ground station is represented by a point object that acts as a forced sink and source of tether length, where the tether is modeled as a one-dimensional massless rigid rod element that is free to rotate about its longitudinal axis. As stated before, the kite is modeled as a rigid body.

The 5 Degrees of Freedom (DOF) of the kite system result from the spherical joint between the ground station and the tether providing 3 rotational DOF, the variable length of the tether and the revolute joint between the tether and the kite. The bridle connection between the tether and the kite constrains the freedom of the kite with respect to the tether and couples the roll and yaw motion as explained in the introduction. The 5 DOF are defined and illustrated in Figs. 2, 3 and 4. The kite system definitions use the inertial Earth reference frame, a tether reference frame, a body reference frame and an aerodynamic reference frame.

Figure 2 displays the ground station and defines the azimuth angle ψ and the zenith angle ϕ. The $-X^E$-axis coincides with the wind vector v_W. The azimuth and zenith angle are the result of subsequent rotation about Z^E and $Y^{E'}$, such that $-Z^T$ coincides with the direction of the tether.

The rotation about the tether's longitudinal axis, addressed as bridle rotation angle χ, is displayed in Fig. 3. The tether length is indicated by l_T. The pitch rotation θ of the revolute joint between the tether and the kite is shown in Fig. 4. To clarify, the bridle rotation angle is such that Y^T is aligned with Y^B.

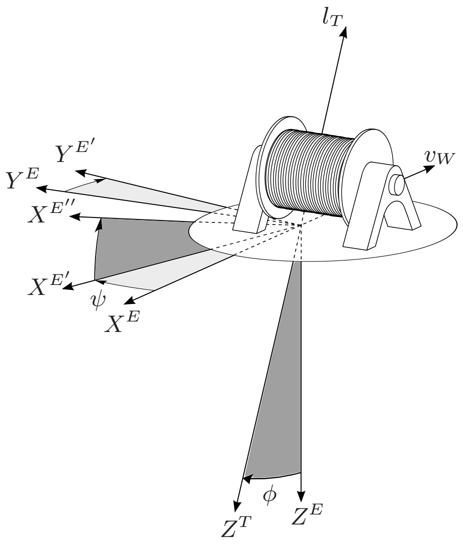

Fig. 2: Definition of the azimuth angle ψ and the zenith angle ϕ.

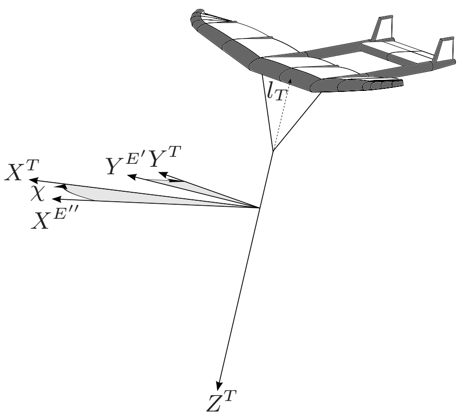

Fig. 3: Definition of the bridle rotation χ.

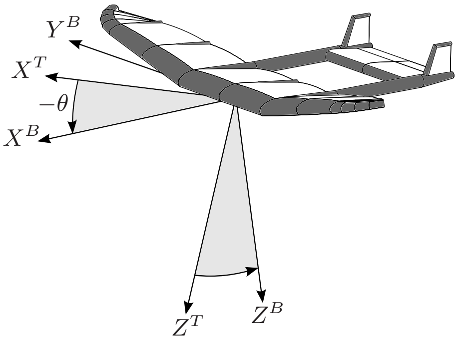

Fig. 4: Definition of the pitch rotation θ.

With the definition that the origin of the body reference frame coincides with the center of gravity (cg), the location of the cg in the Earth reference frame can be expressed as:

$$\mathbf{r}_{cg}^{E} = \mathbb{T}_{ET} \begin{bmatrix} 0 & 0 & -l_T \end{bmatrix}^{\mathrm{T}} + \mathbb{T}_{EB} \begin{bmatrix} -x_T & 0 & -z_T \end{bmatrix}^{\mathrm{T}}. \tag{1}$$

The coordinates x_T and z_T represent the location of the bridle hinge line with respect to the cg, thus to go from the bridle hinge line to the cg they must be subtracted. Expressions for the rotation matrices $\mathbb{T}_{ET}$ and $\mathbb{T}_{EB}$ are constructed from the angle definitions in Figs. 2, 3 and 4.

The aerodynamic reference frame in Fig. 5 is established from the definition that X^a coincides with the apparent velocity vector of the kite through subsequent rotations α about Y^B and β about Z^a. The magnitude of the apparent velocity vector v_{app}, the angle of attack α, the sideslip angle β, and the body angular velocity $\boldsymbol{\omega}_{cg}$ together determine the aerodynamic forces and moments on the kite.

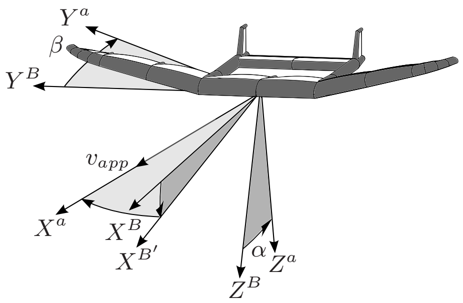

Fig. 5: Definition of the aerodynamic reference frame.

B. Equations of motion

Lagrange's equation of the second kind, Eq. (2), is used to derive five second order differential equations that describe the motion of the kite system.

$$\frac{d}{dt}\frac{\partial T}{\partial \dot{q}_i} - \frac{\partial T}{\partial q_i} + \frac{\partial V}{\partial q_i} = Q_i, \qquad i = 1, \ldots, 5 \tag{2}$$

The five DOF are represented by the generalized coordinates q_i. To evaluate Eq. (2), expressions need to be found for the kinetic energy T, the potential energy V, and the generalized forces Q_i.

The kinetic energy is obtained from Eq. (3) by substituting Eq. (4) for $\mathbf{v}_{cg}$ and Eq. (6) for $\boldsymbol{\omega}_{cg}$.

$$T = \frac{1}{2} m_k \mathbf{v}_{cg} \cdot \mathbf{v}_{cg} + \frac{1}{2} \boldsymbol{\omega}_{cg}^{\mathrm{T}} \cdot \mathbb{I} \cdot \boldsymbol{\omega}_{cg} \tag{3}$$

Equation (4) is found by differentiating $\mathbf{r}_{cg}$ with respect to time and Eqs. (5) and (6) are constructed from the definitions in Section II A.

$$\begin{aligned} \mathbf{v}_{cg}^{T} &= \begin{bmatrix} 0 & 0 & -\dot{l}_T \end{bmatrix}^{\mathrm{T}} + \boldsymbol{\omega}_{E_T}^{T} \times \begin{bmatrix} 0 & 0 & -l_T \end{bmatrix}^{\mathrm{T}} \\ &\quad + \mathbb{T}_{TB} \cdot \boldsymbol{\omega}_{E_B}^{B} \times \begin{bmatrix} -x_T & 0 & -z_T \end{bmatrix}^{\mathrm{T}} \end{aligned} \tag{4}$$

$$\boldsymbol{\omega}_{E_T}^{T} = \begin{bmatrix} 0 \\ 0 \\ \dot{\chi} \end{bmatrix} + \mathbb{T}_{TE''} \begin{bmatrix} 0 \\ \dot{\phi} \\ 0 \end{bmatrix} + \mathbb{T}_{TE'} \begin{bmatrix} 0 \\ 0 \\ \dot{\psi} \end{bmatrix} \tag{5}$$

$$\boldsymbol{\omega}_{E_B}^{B} = \begin{bmatrix} 0 \\ \dot{\theta} \\ 0 \end{bmatrix} + \mathbb{T}_{BT} \begin{bmatrix} 0 \\ 0 \\ \dot{\chi} \end{bmatrix} + \mathbb{T}_{BE''} \begin{bmatrix} 0 \\ \dot{\phi} \\ 0 \end{bmatrix} + \mathbb{T}_{BE'} \begin{bmatrix} 0 \\ 0 \\ \dot{\psi} \end{bmatrix} \tag{6}$$

The potential energy is given by Eq. (7), where m_g represents the kite mass excluding the confined air. To avoid inclusion of buoyancy forces, the confined air mass is subtracted from m_k assuming that the centers of mass coincide.

$$V = m_g \mathbf{g} \cdot \mathbf{r}_{cg} \tag{7}$$

Since the kite system is subjected to nonconservative forces such as aerodynamic and ground station loads, expressions for these forces are required in the form of generalized forces. For a rigid body, the resulting aerodynamic loads can be expressed as a force vector and a moment vector that act on the kite cg. In the body reference frame, these two vectors are denoted by respectively $\mathbf{F}_a^B$ and $\mathbf{M}_a^B$. The force of the ground station acting on the tether is represented by $\mathbf{F}_{GS}^T$ in the tether reference frame.

With the nonconservative forces specified, the generalized force Q_i for generalized coordinate q_i can be derived using the principle of virtual work in Eq. (8).

$$Q_i = \frac{\partial \dot{\mathbf{r}}}{\partial \dot{q}_i} \cdot \mathbf{F} + \frac{\partial \dot{\boldsymbol{\omega}}}{\partial \dot{q}_i} \cdot \mathbf{M}, \qquad i = 1, \ldots, 5 \tag{8}$$

The results of applying Eqs. (8) to the generalized coordinates in the kite system are displayed in Eqs. (9) through (13). Note that the nonconservative forces are transformed to the reference frames corresponding to the generalized coordinates.

$$Q_\theta = \frac{\partial}{\partial \dot{\theta}} \left(\mathbf{M}_a^B \cdot \begin{bmatrix} 0 \\ \dot{\theta} \\ 0 \end{bmatrix} + \mathbf{F}_a^B \cdot \left(\begin{bmatrix} 0 \\ \dot{\theta} \\ 0 \end{bmatrix} \times \begin{bmatrix} -x_T \\ 0 \\ -z_T \end{bmatrix} \right) \right) \tag{9}$$

$$Q_\chi = \frac{\partial}{\partial \dot{\chi}} \left(\mathbf{M}_a^T \cdot \begin{bmatrix} 0 \\ 0 \\ \dot{\chi} \end{bmatrix} + \mathbf{F}_a^T \cdot \left(\begin{bmatrix} 0 \\ 0 \\ \dot{\chi} \end{bmatrix} \times \begin{bmatrix} -x_T \\ 0 \\ -z_T \end{bmatrix} \right) \right) \tag{10}$$

$$Q_{l_T} = \frac{\partial}{\partial \dot{l}_T} \left(\left(\mathbf{F}_a^T + \mathbf{F}_{GS}^T \right) \cdot \begin{bmatrix} 0 \\ 0 \\ -\dot{l}_T \end{bmatrix} \right) \tag{11}$$

$$Q_\phi = \frac{\partial}{\partial \dot{\phi}} \left(\mathbf{M}_a^{E''} \cdot \begin{bmatrix} 0 \\ \dot{\phi} \\ 0 \end{bmatrix} + \mathbf{F}_a^{E''} \cdot \left(\begin{bmatrix} 0 \\ \dot{\phi} \\ 0 \end{bmatrix} \times \mathbf{r}_{cg}^{E''} \right) \right) \tag{12}$$

$$Q_\psi = \frac{\partial}{\partial \dot{\psi}} \left(\mathbf{M}_a^{E'} \cdot \begin{bmatrix} 0 \\ 0 \\ \dot{\psi} \end{bmatrix} + \mathbf{F}_a^{E'} \cdot \left(\begin{bmatrix} 0 \\ 0 \\ \dot{\psi} \end{bmatrix} \times \mathbf{r}_{cg}^{E'} \right) \right) \tag{13}$$

C. Aerodynamic model

In the generalized forces, the aerodynamics are incorporated through the force vector $\mathbf{F}_a$ and moment vector $\mathbf{M}_a$. However, an expression for these vectors is yet to be found. For this purpose, an aerodynamic element discretization is employed to acquire a parametric model in terms of the geometric properties. The basic idea, illustrated by Fig. 6, is to calculate the aerodynamic forces locally at the aerodynamic elements and then calculate the contribution to $\mathbf{F}_a^B$ and $\mathbf{M}_a^B$ based on the position and orientation of the element in the body reference frame.

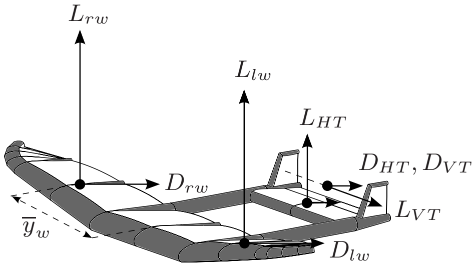

Fig. 6: Illustration of the aerodynamic element discretization.

An advantage of this approach is that it avoids estimations of stability derivatives because they are in fact accounted for by the relative location and orientation of the aerodynamic elements. In fact, they result from lower level estimations at the aerodynamic elements. This approach then yields the aerodynamics tree in Fig. 7, which implementation is discussed in the following.

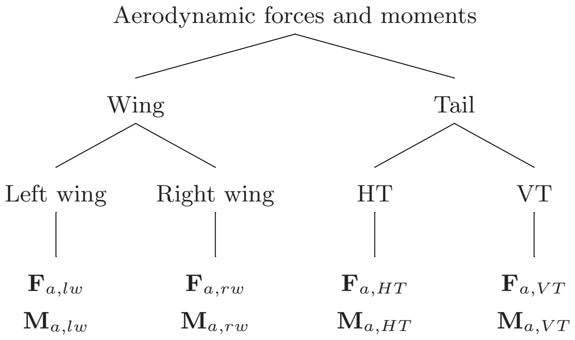

Fig. 7: Aerodynamics forces and moments breakdown.

Wing aerodynamics. To incorporate the dihedral angle as a parameter in the model, the wing is split up in two aerodynamic elements, left and right. For the calculation of the lift and drag force on the wing halves, the airflow is observed at the quarter cord point of the spanwise mean aerodynamic cord (MAC) location ($\overline{y}_w$). It is assumed that this point best represents the wing half. By splitting the wing, the effect of dihedral and rotational velocities on the aerodynamic forces and moments is automatically taken into account. The apparent velocity at the MAC location on the right wing is given by Eq. (14), a similar result can be obtained for the left wing.

$$\mathbf{v}^B_{a,rw} = \mathbf{v}^B_{a,cg} + \boldsymbol{\omega}^B_{cg} \times \begin{bmatrix} x_{LE} - \frac{1}{4}\overline{c}_w \\ \overline{y}_w \cos(\Gamma) \\ -\overline{y}_w \sin(\Gamma) \end{bmatrix} \tag{14}$$

The global aerodynamic angles α and β are defined, as usual, according to Eqs. (15) and (16) respectively.

$$\alpha = \arctan\left(\frac{v^B_{a,Z}}{v^B_{a,X}}\right) \tag{15}$$

$$\beta = \arctan\left(\frac{v^B_{a,Y}}{\sqrt{{v^B_{a,X}}^2 + {v^B_{a,Z}}^2}}\right) \tag{16}$$

However, to find the local aerodynamic angles, a transformation is required to account for the rotation of the aerodynamic element about X^B. Equation (17) provides the transformation matrix for a positive rotation ζ about X^B. For example, when a straight right wing half is rotated 90°, the positive β becomes a negative local angle of attack and the positive α becomes a positive sideslip angle.

$$\begin{bmatrix} \alpha_l \\ \beta_l \end{bmatrix} = \begin{bmatrix} cos(\zeta) & -sin(\zeta) \\ sin(\zeta) & cos(\zeta) \end{bmatrix} \cdot \begin{bmatrix} \alpha \\ \beta \end{bmatrix} \tag{17}$$

In the case of the right wing half ζ is equal to $-\Gamma$, and for the left half ζ is equal to Γ. For the calculation of the lift and drag on the wing halves, experimental or theoretical $C_L - \alpha$ and $C_D - \alpha$ curves can be used to link the local aerodynamic angles to aerodynamic coefficients. In the Kiteplane case study, experimental data from [30] is combined with the approach for 3D plates at an angle from [31] to obtain the curves in Fig. 8.

The lift and drag of the right wing half are then calculated using Eqs. (18) and (19). The expressions for the left wing half are similar.

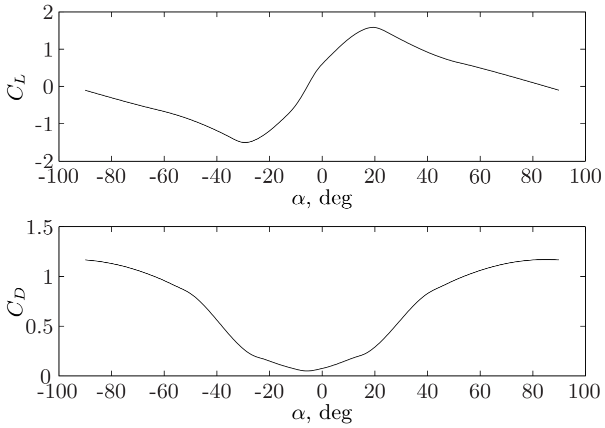

Fig. 8: $C_L - \alpha$ and $C_D - \alpha$ curves for the Kiteplane wing.

$$L_{rw} = \frac{1}{2}\rho \mathbf{v}^B_{a,rw} \cdot \mathbf{v}^B_{a,rw} C_L \frac{S_w}{2} \tag{18}$$

$$D_{rw} = \frac{1}{2}\rho \mathbf{v}^B_{a,rw} \cdot \mathbf{v}^B_{a,rw} C_D \frac{S_w}{2} \tag{19}$$

The resulting lift and drag force are used in Eqs. (20) and (21) to calculate the contribution of the right wing halve to $\mathbf{F}^B_a$ and $\mathbf{M}^B_a$. Note that the local aerodynamic angles are used for the transformation $\mathbb{T}_{Ba}$. Similar expressions are obtained for the left wing half.

$$\mathbf{F}^B_{a,rw} = \mathbb{T}_{Ba} \begin{bmatrix} -D_{rw} \\ 0 \\ -L_{rw} \end{bmatrix} \tag{20}$$

$$\mathbf{M}^B_{a,rw} = \begin{bmatrix} x_{LE} - \frac{1}{4}\overline{c}_w \\ \overline{y}_w \cos(\Gamma) \\ -\overline{y}_w \sin(\Gamma) \end{bmatrix} \times \mathbb{T}_{Ba} \begin{bmatrix} -D_{rw} \\ 0 \\ -L_{rw} \end{bmatrix} \tag{21}$$

If the wing has a nonzero pitching moment, this can be included separately using Eq. (22), provided that a value or curve for $C_{m_{ac}}$ is available.

$$M_{w_{ac}} = \frac{1}{2}\rho \mathbf{v}^B_a \cdot \mathbf{v}^B_a S_w \overline{c}_w C_{m_{ac}} \tag{22}$$

Horizontal tail plane aerodynamics. The contribution of the horizontal tail plane to the aerodynamic forces and moments is calculated essentially in the same way as the contribution of the wing. There are, however, some differences, because the local angle of attack is different from the global angle of attack due to the incidence angle of the horizontal tail plane and the downwash from the wing. The derivative of the downwash angle with respect to the angle of attack $\frac{d\epsilon}{d\alpha}$ can, for example, be estimated using the empirical methods in [32]. The angle of attack at the horizontal tail plane is then calculated using Eq. (23).

$$\alpha_{HT} = \alpha_l - \frac{d\epsilon}{d\alpha}\alpha + i_{HT} \tag{23}$$

The α_l in Eq. (23) needs to be calculated based on the local apparent velocity, which is calculated using Eq. (24).

$$\mathbf{v}^B_{a,HT} = \mathbf{v}^B_{a,cg} + \boldsymbol{\omega}^B_{cg} \times \begin{bmatrix} x_{LE} - \frac{1}{4}\overline{c}_w - l_{HT} \\ 0 \\ 0 \end{bmatrix} \tag{24}$$

With the obtained value for α_{HT}, the lift and drag coefficients can be found using estimated $C_L - \alpha$ and $C_D - \alpha$ curves. The lift and drag force on the horizontal tail plane are calculated using Eqs. (25) and (26), where the term $(v_t/v)^2$ accounts for the velocity loss due to the presence of the wing.

$$L_{HT} = \frac{1}{2}\rho \mathbf{v}^B_{a,HT} \cdot \mathbf{v}^B_{a,HT} \left(\frac{v_t}{v}\right)^2 C_L S_{HT} \tag{25}$$

$$D_{HT} = \frac{1}{2}\rho \mathbf{v}^B_{a,HT} \cdot \mathbf{v}^B_{a,HT} \left(\frac{v_t}{v}\right)^2 C_D S_{HT} \tag{26}$$

Using these lift and drag values, the contribution of the horizontal tail plane to $\mathbf{F}^B_a$ and $\mathbf{M}^B_a$ is obtained from Eqs. (27) and (28). Again, the local α and β angles are to be used for the $\mathbb{T}_{Ba}$ transformation.

$$\mathbf{F}^B_{a,HT} = \mathbb{T}_{Ba} \begin{bmatrix} -D_{HT} \\ 0 \\ -L_{HT} \end{bmatrix} \tag{27}$$

$$\mathbf{M}^B_{a,HT} = \begin{bmatrix} x_{LE} - \frac{1}{4}\overline{c}_w - l_{HT} \\ 0 \\ 0 \end{bmatrix} \times \mathbb{T}_{Ba} \begin{bmatrix} -D_{HT} \\ 0 \\ -L_{HT} \end{bmatrix} \tag{28}$$

Vertical tail plane aerodynamics. As with the other elements, a single resultant force is calculated at the quarter cord point of the spanwise MAC location. In the Kiteplane case study there are in fact two vertical fins, which are approximated by a single element using the fins original MAC location and aerodynamics properties, but taking into account twice the size. Due to the simplifications in the model, this is equal to including both fins separately when the small effect of the lateral position of the fins on the distance to the equivalent vertical tail plane is neglected. The local velocity at the vertical tail plane is given by Eq. (29).

$$\mathbf{v}^B_{a,VT} = \mathbf{v}^B_{a,cg} + \boldsymbol{\omega}^B_{cg} \times \begin{bmatrix} x_{LE} - \frac{1}{4}\overline{c}_{VT} - l_{VT} \\ 0 \\ z_{LE} - \overline{z}_{VT} \end{bmatrix} \tag{29}$$

Since the vertical tail plane element is rotated -90° about the X_B-axis, the angle of attack for the vertical tail plane is equal to the sideslip angle resulting from Eq. (16).

With α_{VT} determined, the lift and drag coefficients can again be obtained from estimated $C_L - \alpha$ and $C_D - \alpha$ curves. The lift and drag force on the vertical tail plane are calculated with equations similar to Eqs. (25) and (26), and inserted in Eqs. (30) and (31) to find the contribution to $\mathbf{F}^B_a$ and $\mathbf{M}^B_a$.

$$\mathbf{F}^B_{a,VT} = \mathbb{T}_{Ba} \begin{bmatrix} -D_{VT} \\ -L_{VT} \\ 0 \end{bmatrix} \tag{30}$$

$$\mathbf{M}^B_{a,VT} = \begin{bmatrix} x_{LE} - \frac{1}{4}\overline{c}_w - l_{VT} \\ 0 \\ z_{LE} - \overline{z}_{VT} \end{bmatrix} \times \mathbb{T}_{Ba} \begin{bmatrix} -D_{HT} \\ -L_{HT} \\ 0 \end{bmatrix} \tag{31}$$

D. Ground station force

Since the tether is modeled as a massless rigid one-dimensional rod, the ground station accounts for the spring damper dynamics. This approach combines the tether dynamics and ground station dynamics in a single force. The ground station force that represents the spring damper dynamics of a fixed length tether is given by Eq. (32), where k represents the spring constant and d the damping constant. Both properties depend on the tether material, thickness and length.

$$F_{GS} = \begin{cases} k\left(l_T - l_{T0}\right) + d\dot{l}_T, & l_T \geq l_{T0} \\ 0, & l_T < l_{T0} \end{cases} \tag{32}$$

III. Results of the Kiteplane case study

With the described methodology, analytical as well as numerical results can be obtained for various aircraft shaped kites. In this paper a case study is preformed on a specific kite, the Kiteplane, to investigate whether the developed model can describe its dominating behavior. The Kiteplane, displayed in previous figures, features an approximate elliptic wing with positive dihedral from the tail boom section to the tips and is in size comparable to a small surfkite. The twin tail booms support the horizontal tail plane that is located in between and the two vertical tail planes on top. The main geometrical properties are listed in Table 1, where the MAC and its location are calculated using the definitions from [33].

The inertia of the Kiteplane consists of three parts: the pressurized beam structure, the canopy surfaces, and the air confined in the tubes and airfoils. The contribution of displaced air is assumed

Table 1: Geometric properties of the Kiteplane.

Component	Parameter	Symbol	Value	Unit
Wing	Surface area	S_w	5.67	m^2
	Aspect ratio	A_w	5.65	
	Taper ratio	λ	0.66	
	Dihedral angle[1]	Γ	14	Deg
	MAC	$\overline{c}_w$	1.08	m
	MAC location	$\overline{y}_w$	1.21	m
Airframe	Total length	l	3.08	m
	HT distance	l_{HT}	2.24	m
	VT distance	l_{VT}	2.56	m
HT	Surface area	S_{HT}	1.28	m^2
	Aspect ratio	A_{HT}	2.2	
	MAC	$\overline{c}_{HT}$	0.76	m
VT	2 × surface area	S_{VT}	0.33	m^2
	Aspect ratio	A_{VT}	1.2	
	Taper ratio	λ_{VT}	0.59	
	LE sweep	$\Lambda_{LE,VT}$	23	Deg
	MAC	$\overline{c}_{VT}$	0.38	m
	MAC location	$\overline{y}_{VT}$	0.20	m

[1] Of the outer wing.

to be negligible, because the Kiteplane is still about five times heavier than air. Estimations based on the CAD model give the following properties:

$$m_k = 4.21 \text{ kg}, \quad m_g = 3.44 \text{ kg},$$

$$\mathbf{r}_{LE}^{B} = \begin{bmatrix} 0.916 & 0 & 0.089 \end{bmatrix}^{\mathrm{T}} \text{m},$$

$$\mathbb{I} = \begin{bmatrix} 7.38 & 0 & 0.18 \\ 0 & 4.20 & 0 \\ 0.18 & 0 & 11.43 \end{bmatrix} \text{kgm}^2.$$

The vector $\mathbf{r}_{LE}^{B}$ represents the position of the LE with respect to the cg in the body reference frame. Apparently, the center of gravity is located at about 92 cm behind the leading edge of the wing, this is at approximately 85% of the MAC.

A. Analytical stability analysis

By examining the free body diagram of the kite, the static stability of distinct motions of the system can be determined. However, when the kite is located in the plane spanned by the wind velocity v_W and the vertical, the symmetry plane, the results are equivalent to that of a regular airplane. The only difference, the tether force, acts in this case as additional gravity and thrust. This situation can be viewed as gliding flight.

Application of airplane stability analysis as described by e.g. [34–36] to the Kiteplane, yields longitudinal static stability in the symmetry plane if $v_W > 3$ m/s depending on the angle of attack. Although the aerodynamic center (ac) of the Kiteplane is located at approximately $l_{HT}\frac{S_{HT}}{S} = 0.51$ m behind the wing ac, or 15 cm in front of the cg, the tether force moves the apparent cg in front of the aerodynamic center if the lift excesses exceeds the weight. The results of the longitudinal stability analysis are summarized in Fig. 9, which shows the pitch and zenith angle equilibrium in ϕ-α space. The arrows give an indication of the convergence.

The angle of attack that satisfies pitch equilibrium does not depend on ϕ and is therefore a straight line. The equilibrium in zenith angle is more interesting because it is equivalent to the L/D, including weight effects, for a specific angle of attack and wind velocity. The maximum L/D, or minimal equilibrium ϕ, is achieved at $\alpha \approx 8°$. However, these equilibrium lines will shift if the operating conditions change. For example, a higher wind velocity reduces the relative effect of gravity and this will cause the solid line to shift to the left for a higher L/D and the dashed line downwards for a lower lift coefficient.

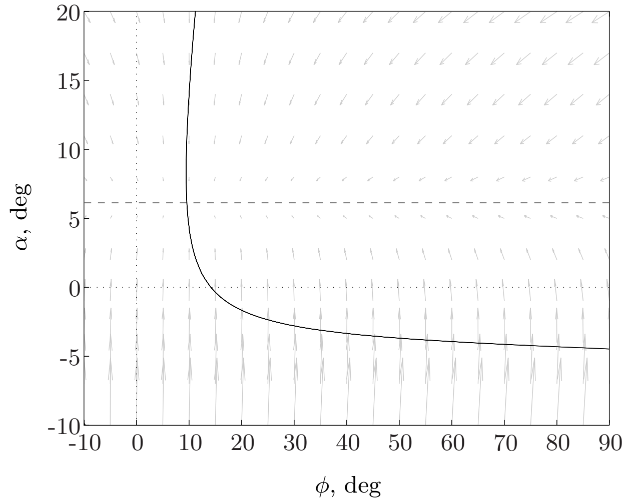

Fig. 9: Static longitudinal stability with zenith equilibrium — and pitch equilibrium −−.

Lateral stability analysis in the symmetry plane, without lateral components of the tether force and gravity, shows that the Kiteplane is statically stable in pure roll (low elevation) and pure yaw (high elevation). Because positive rotation about X^B initiates positive rotation about Z^B and vice versa, rotation about Z^T is a statically stable combination of the investigated extremes. Furthermore, sideslipping is dynamically stable.

If the kite moves outside the symmetry plane, the situation is fundamentally different from airplane motion due to the constraints posed by the fixed length tether and the bridle connection. In this condition, the tether force and gravity start to interfere in the roll and yaw motion of the kite. To investigate the stability of this motion the reduced model displayed in Fig. 10, with the two DOF θ_T and χ, is analyzed.

Pendulum stability requires the Kiteplane to converge to the situation displayed in Fig. 10 from a disturbance in θ_T. To investigate the pendulum stability, the situation in Fig. 11 is considered. This is a typical scenario where, for the observer, the Kiteplane is located on the left side and falling to the left side. It is assumed that χ changes such that the Kiteplane always points approximately into the wind ($-X^E$), because then the lateral force F_Y^B is tangential to the pendulum arc and relates directly to θ_T. This assumption restrains the DOF χ, but aerodynamically the rotation

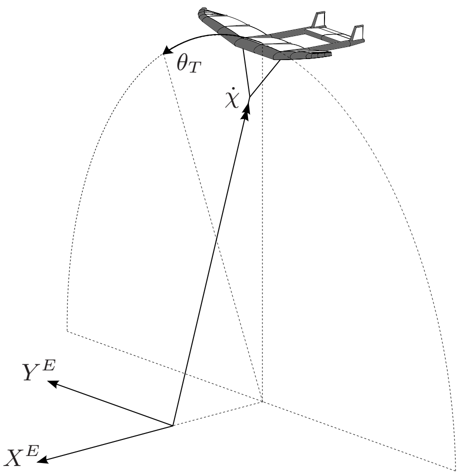

Fig. 10: Kiteplane system pendulum motion.

about Z^T is governed by β, which is free and replaces χ as the second DOF. The sum of the lateral forces is given by Eq. (33). The sum of moments about X^B and Z^B, evaluated at the tether attachment point located below the wing ac, are given by Eqs. (34) and (35) respectively. The minor impact of the horizontal tail lift and drag force on the pendulum motion is neglected.

$$\begin{aligned}\sum F_Y^B &= -2\left(L_f\cos(\beta) + D_f\sin(\beta)\right) - Y_{rw} + Y_{lw} + \\ &\quad F_Z\sin(\theta_T) \qquad (33)\\ \sum M_X^B &= \left(L_{lw} - L_{rw}\right)\overline{y}_w + \left(F_{B_r} - F_{B_l}\right)y_b\cos(\delta) - \\ &\quad 2\left(L_f\cos(\beta) + D_f\sin(\beta)\right)\left(\overline{y}_{VT} + z_T\right) + \\ &\quad F_Z\sin(\theta_T)z_T \qquad (34)\\ \sum M_Z^B &= \left(X_{rw} - X_{lw}\right)\overline{y}_w\cos(\Gamma) - F_Z\sin(\theta_T)x_T + \\ &\quad 2\left(L_f\cos(\beta) + D_f\sin(\beta)\right)l_{VT} \qquad (35)\end{aligned}$$

In Eqs. (33) through (35), the lift and drag of the wing halves has been converted to X and Y components. The wing dihedral causes a difference in angle of attack between the wing halves, therefore the lift and drag cannot be conveniently captured in the body reference frame. Figure 12 provides an indication of the variation in force coefficients C_{X_w} and C_{Y_w} with β in case $\alpha = 5°$.

The lift and drag forces in Eqs. (33) through (35) are obtained using the common aerodynamic

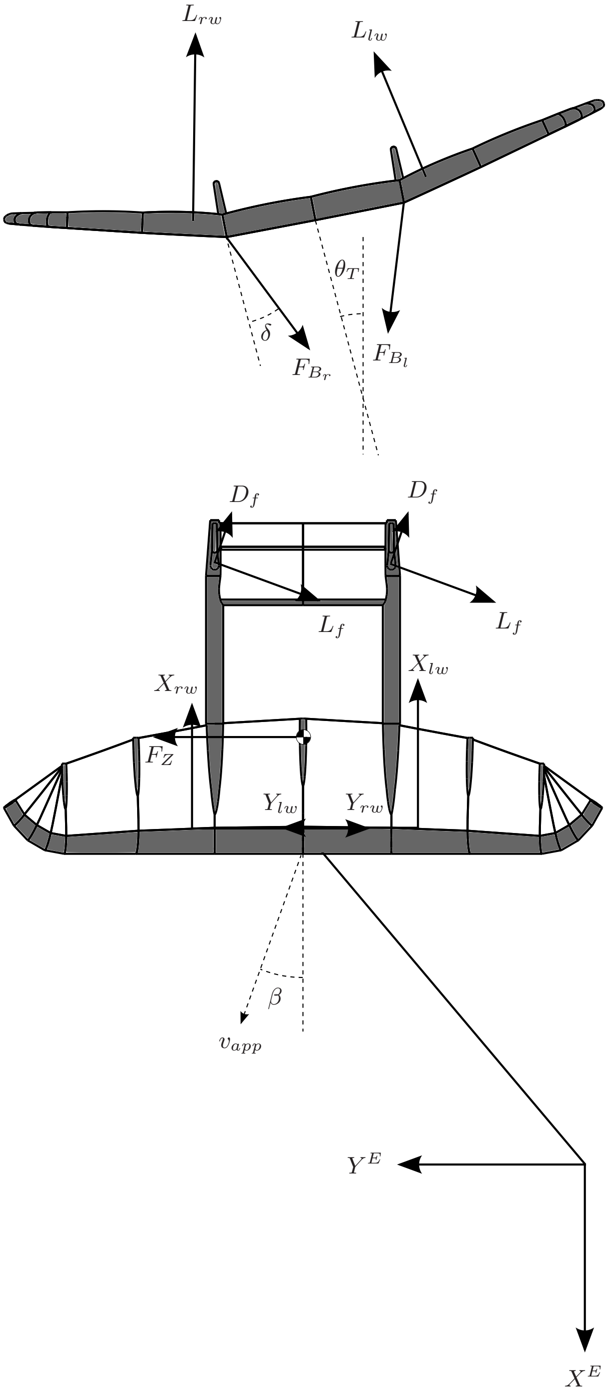

Fig. 11: Front and top view of the Kiteplane in pendulum motion.

relations in Section II C. The forces like X_{rw} are calculated similarly, but now the drag coefficient is for example replaced by $C_{X_{rw}}$. Note that these forces are simply transformations of lift and drag. The gravitational force F_Z is found by multiplying m_g with the gravitational acceleration.

To find quantitative results for the pendulum stability, the following case constants are intro-

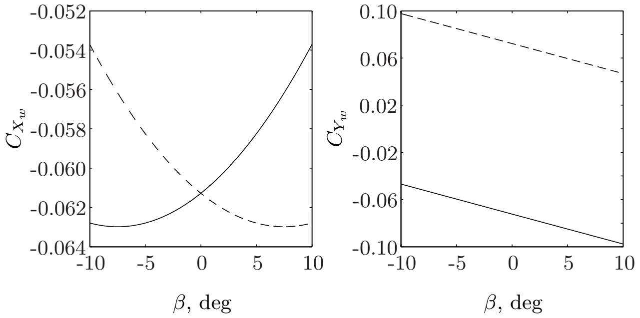

Fig. 12: C_{X_w} and C_{Y_w} for the right wing — and left wing −− as a function of β with $\alpha = 5°$.

duced:

$$\begin{array}{rcrlrcrl} \rho & = & 1.225 & \text{kgm}^{-3}, & g & = & 9.81 & \text{ms}^{-2}, \\ x_T & = & 0.65 & \text{m}, & \frac{v_t}{v} & = & 0.95, & \\ z_T & = & 0.2 & \text{m}, & v_W & = & 6 & \text{m/s}, \\ \alpha & = & 5 & \text{deg}, & \theta & = & -5 & \text{deg}. \end{array}$$

Because the pendulum motion is a combination of θ_T and β, strictly necessary conditions for static stability are difficult to define, however, four sufficient conditions can be formulated using Eq. (36).

$$\begin{aligned} dF_Y^B/d\theta_T &< 0 \\ dF_Y^B/d\beta &< 0 \\ dM_Z^T/d\theta_T &< 0 \\ dM_Z^T/d\beta &> 0 \end{aligned}$$

$$M_Z^T = M_Z^B cos(\theta) + M_X^B sin(-\theta) \tag{36}$$

With the case constants substituted, F_Y^B and M_Z^T can be plotted as functions of θ_T and β. Figure 13 displays the lines $F_Y^B = 0$ and $M_Z^T = 0$ in θ_T-β space. The lines represent the equilibrium condition for Y^B and Z^T. The only equilibrium for the pendulum motion is found at the point (0,0) in Fig. 13, which is the trivial equilibrium in the symmetric plane. The arrows in Fig. 13 indicate in which direction the Kiteplane is accelerated. They are, in steady state, a measure for the acceleration vector in θ_T-β space with x-component $\ddot{\theta}_T$ and y-component $\ddot{\beta}$.

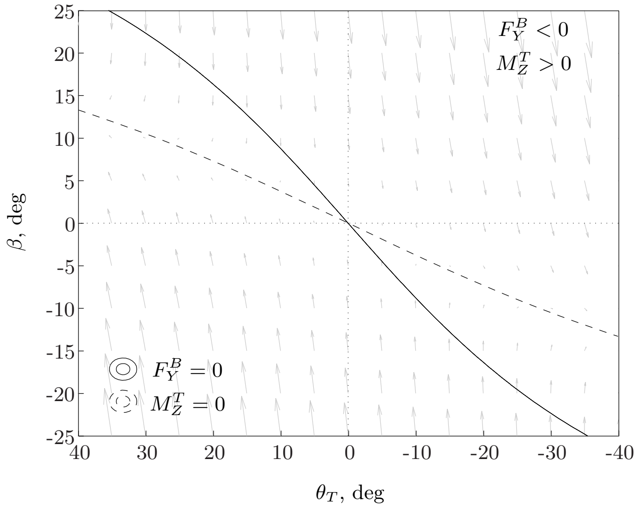

Fig. 13: Pendulum stability with θ_T equilibrium — and β equilibrium $--$.

Figure 14 displays horizontal and vertical slices of Fig. 13. Figure 14a displays a horizontal slice at $\beta = 10°$ and Fig. 14b a vertical slice at $\theta_T = 20°$ (right), which gives an impression of the gradients. Observation of the gradients yields the conclusion that three out of four of the sufficient conditions for static pendulum stability are met. The derivative $dF_Y^B/d\theta_T$ is positive instead of negative.

Nonetheless, if a positive equilibrium β results in a negative value for F_Y^B, the system may still be stable. This means that in Fig. 13 the dashed M_Z^T line should be steeper than the solid F_Y^B line, but this is neither the case. Similar conclusions can be drawn from following the arrows in Fig. 13, which results in diverging either to the left or to the right.

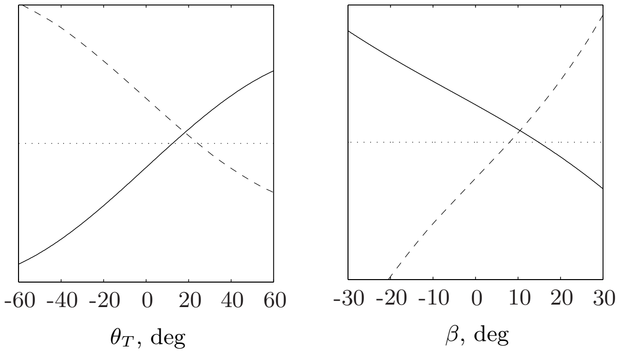

(a) Slice at $\beta = 10°$

(b) Slice at $\theta_T = 20°$

Fig. 14: F_Y^B — and M_Z^T $--$ for two slices in θ_T-β space.

The analysis in this section proves that the Kiteplane system restricted to pendulum motion is unstable. This cannot be guaranteed for the unrestricted Kiteplane system, but it is nevertheless likely that it exhibits some of this unstable behavior. The investigation of this pendulum motion is continued trough numerical simulation.

B. Numerical simulation results

To study the motion of the Kiteplane, numerical simulations are produced with a MATLAB/Simulink model that is constructed from the derived equations of motion. The model is used to solve initial value problems, which results can subsequently be compared to other simulations or flight tests. The structure of the model is displayed in Fig. 15, each block represents a procedure or a subset of procedures. The procedure that calculates the second order time derivatives of the generalized coordinates is for example represented by the $\ddot{q}$ block. The actual model that calculates the motion of the Kiteplane system consists of the blocks that are enclosed by the dashed line. The blocks Constants and $\mathbf{x}_0$ are inputs for the model and the blocks Dashboard and $\mathbf{x}$ tracking are the outputs.

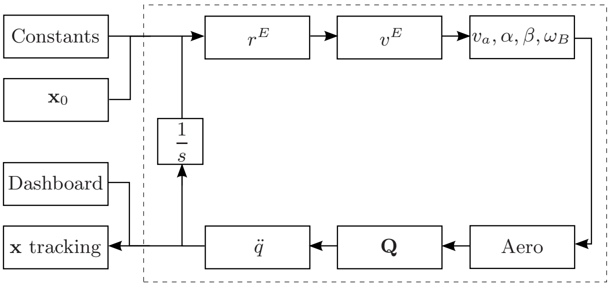

Fig. 15: Global structure of the numerical model.

With the input, first the position of the cg is calculated in the Earth reference frame by the block r^E. The second operation is to calculated the velocity in the Earth reference frame, this is done by the block $\mathbf{v}^E$. By combining $\mathbf{v}^E$ and the wind velocity from the input data, the aerodynamic states v_{app}, α, β and $\boldsymbol{\omega}_B$ are determined by the eponymous block. This block concludes the preparing calculations to solve the equations of motion.

In the Aero block, the aerodynamic force vector $\mathbf{F}_a^B$ and the aerodynamic moment vector $\mathbf{M}_a^B$ are calculated based on the aerodynamic states. The $\mathbf{Q}$ block calculates the ground station force, adds it to the aerodynamics forces, and converts the sum to a generalized force for each of the five generalized coordinates. The second derivatives of the generalized coordinates are calculated by the $\ddot{q}$ block. The $\frac{1}{s}$ block concludes the time step by integrating the state vector derivative to find the new state. After this, the whole procedure is repeated until the time reaches the predefined end time of the simulation.

Flight test comparison. To test the validity of the model, a typical test flight is reconstructed. The state of the Kiteplane after the launch is estimated from flight test footage and fed into the model as initial conditions. The simulated motion and estimated initial conditions are displayed in Fig. 16. The corresponding flight test footage is shown in Fig. 17 for comparison. The 3D flight path displayed in Fig. 16 is similar to that in Fig 17, but the motion takes 40% more time in the simulation. This is a significant difference, but both seem to show the same instability.

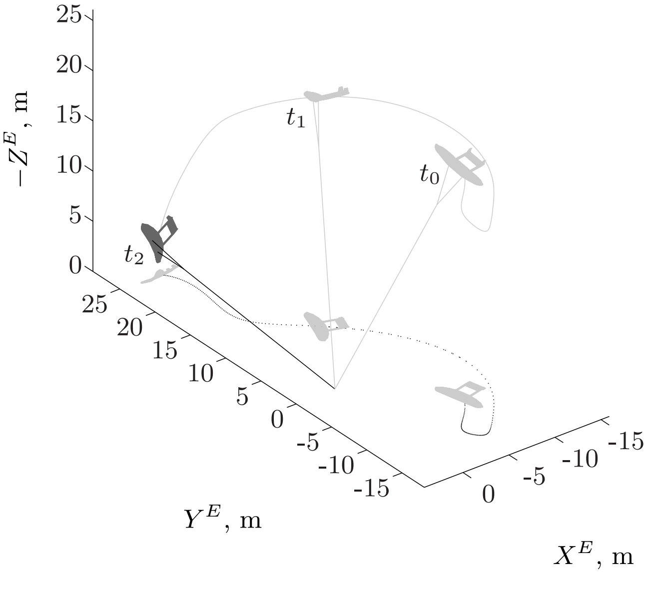

Fig. 16: 3D path of diverging motion with asymmetric and static initial conditions: $\theta = -10°$, $\chi = -60°$, $l_T = 25$ m, $\phi = 25°$, $\psi = 45°$, and $\Delta t = 17$ s.

Due to the initial sideslip angle, the Kiteplane starts moving in the $-Y^E$ direction and rotating about the Z^T axis. At 4 s, the Kiteplane reaches its maximum ψ angle and slowly starts moving in Y^E direction. Due to the high inertia in Y^E motion compared to the inertia in Z^T rotation, the Kiteplane is already highly rotated before the motion in Y^E direction gains momentum. This behavior causes the Kiteplane to reach a sideslip angle of almost -40° at $t = 6$ s. From this point

Fig. 17: Composite photo constructed from flight test footage with $v_W \approx 6$ ms^{-1}, the flight time captured in this figure is approximately 12 s.

on, the Kiteplane starts accelerating in Y^E direction with increasing α, increasing v_{app} and quickly reducing β. At the passing of $-X^E$, the same inertia that initially kept the Kiteplane from returning to $\psi = 0$ is now causing a major overshoot in ψ. At about 11 s, the Kiteplane is pushed toward a point of no return and falls to the ground. The increase in β at this point is insufficient to generate a large enough aerodynamic force in $-Y^B$ direction to overcome the gravity component in Y^B direction.

The pendulum motion that was studied analytically in the previous section seems dominant in this flight and it appears that the analytical approach as well as the simulation agree on the instability that is observed in reality. A comparison of the simulation and the analytical pendulum analysis is displayed in Fig. 18. The simulated trajectory in θ_T-β space is indicated by the gray line, with the circle mark as starting point and the cross mark as final state.

As explained previously, a position above and to the right of the solid and dashed black lines yields respectively a negative force in Y^B and a positive moment about Z^T. Similarly, a position below and to the left of the solid and dashed black lines yields respectively a positive force in Y^B and a negative moment about Z^T. The magnitude of the force and moment increases with distance from the equilibrium lines. The arrows show approximately the local acceleration vector in θ_T-β space and are therefore the most intuitive means to determine the expected direction of motion.

Thus, in the starting condition, F^B_Y is negative and M^T_Z is positive. This is in correspondence with the motion displayed in Fig. 16. Subsequently, this motion causes the Kiteplane to move to

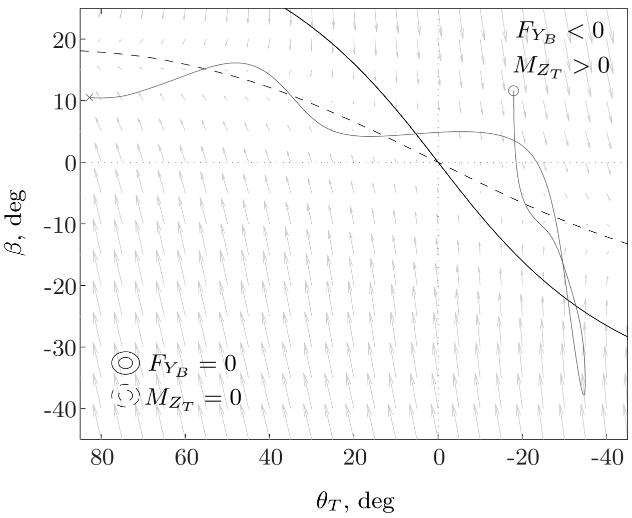

Fig. 18: Pendulum static stability applied to diverging motion — with asymmetric and static initial conditions: $\theta = -10°$, $\chi = -60°$, $l_T = 25$ m, $\phi = 25°$, $\psi = 45°$, and $\Delta t = 17$ s.

another position in θ_T-β space where F_Y^B is positive and M_Z^T is negative. This in turn causes the Kiteplane to move in the direction of Y^E with increasing velocity. This increase in velocity reduces the inertia effects compared to the aerodynamic effects and the gray line start to converge toward the dashed black line in the upper right quadrant. However, the equilibrium sideslip angle does never result in a sufficient large sideslip angle for θ_T to convergence. While the sideslip angle is slowly converging, the Kiteplane is falling to the side.

From the acceleration arrows alone, one would expect the Kiteplane to fall to the right side by converging to the dashed black line on the right. At first the gray line seems to do exactly that, but at a certain point the line shoots downwards in the area that pushes the Kiteplane back to the middle. Apparently, not all important effect are described by the static 2 DOF approximation. This could be expected because the assumptions that the apparent wind velocity is equal to the wind velocity, the heading coincides roughly with X^E, the body rotational velocities are small, and the roll-yaw coupling is constant, do not hold throughout this flight trajectory.

Moreover, it appears that in reality the asymmetric motion is more stable than Fig. 18 suggests. Due to the inertia in rotation about the tether, the sideslip convergence can be either periodic or aperiodic. If the sideslip motion is periodically converging, the overshoot that causes the heading of the Kiteplane to point toward the middle triggers the symmetric motion. This leads to mixing of the unstable asymmetric motion with the stable symmetric motion, which increases the apparent lateral stability.

If the dashed line in Fig. 18 is relatively steep, i.e. sideslip equilibrium is achieved at high sideslip angles, the Kiteplane tends to rotate more, and this induces the mixing of symmetric and asymmetric motion. A relatively flat solid line, which it is not in this case, allows more time for rotation and hence increases apparent lateral stability. In fact, the Kiteplane system can be stable even when the solid line is slightly steeper than the dashed line.

To summarize, the validity of the static 2 DOF analysis is limited, but it does provide useful insights in the cause of the instability. It seems essential to have a small enough vertical tail plane to achieve a large enough equilibrium sideslip angle, and a large enough lateral area to generate a strong enough lateral force. To test this hypothesis, simulations are run with various vertical tail plane sizes and dihedral angles.

Impact of design variations on stability. Inspection of Table 1 yields many geometrical parameters to investigate, but only the ones with the largest impact on the stability are really interesting for the scope of this paper. The main parameters for longitudinal stability are $\frac{S_{HT}}{S_w}$ and $\frac{l_{HT}}{\bar{c}}$. Since this case study is on the Kiteplane, the wing dimensions are kept constant for convenience and varying S_{HT} and l_{HT} is therefore equivalent to varying the ratios.

Figure 19 shows the effect of reducing the tail boom length on longitudinal stability. The trajectory indicated by the gray lines is the launch motion, where the dashed line represents that for the original size. The effect of reducing S_{HT} by 20% yields similar results. Apparently, the horizontal tail plane contribution can be reduced without jeopardizing stability, the 20% reduction even decreases the overshoot in ϕ significantly.

For the lateral stability, the interesting parameters are S_{VT}, l_{VT} and Γ. Next to these parameters, the inclusion of an additional lateral surface on top or below the wing is regarded interesting as well. The main effect of such a surface can be achieved with dihedral as well, but secondary effects are inherently different. The most noticeable difference is the effect of dihedral on the yaw moment, which is absent for a single vertical surface in the middle of the Kiteplane.

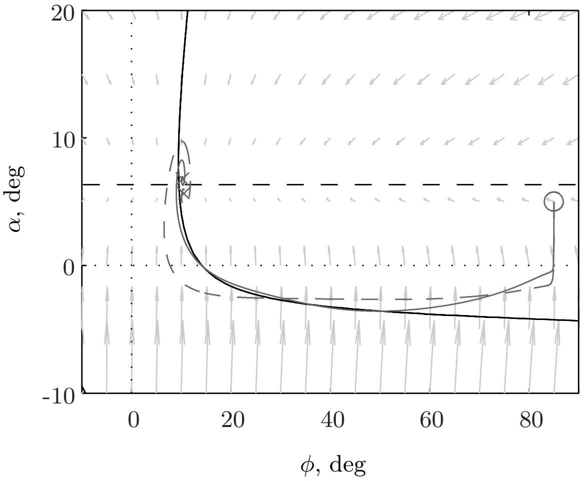

Fig. 19: Effect of 20% reduction in tail boom length on longitudinal stability during launch, original length −− and reduced length —.

Nevertheless, the parameters S_{VT} and Γ are selected for the lateral stability investigation. Keeping the tail boom length constant avoids side effects on longitudinal stability and adjusting Γ is simply found more elegant than the addition of a vertical surface. The impact of variations in S_{VT} and Γ on the inertia is neglected to keep the results depending on geometry only. The effects due to changing inertia are investigated at a later stage.

The stability is assessed based on simulation results in the range $-10° < \Gamma < 40°$ and $0 < \frac{S_{VT}}{S_{VT0}} < 8$ for two different wind velocities. The arrangements of the stability domains are displayed in Fig. 20. Basically, small vertical tail planes cause diverging oscillations and low dihedral angles cause aperiodic divergence. Stability requires a large dihedral angle and a vertical tail plane of about 1 to 3 times the original size. Furthermore, the stable domain increases with increasing wind velocity.

For low dihedral angles and low wind velocities, increasing the vertical tail size leads from unstable oscillations to aperiodic divergence. If the dihedral angle and wind velocity are large enough, a stable regime emerges in between. The stable regime itself consists of three domains. The first, for a small vertical tail plane, is the stable oscillation. The second, for a medium sized vertical tail plane, is the converging oscillation. For large vertical tail planes and low dihedral angles, a domain of aperiodic convergence exists. For higher wind velocities the aperiodic convergence domain increases in size at the cost of the converging oscillation domain.

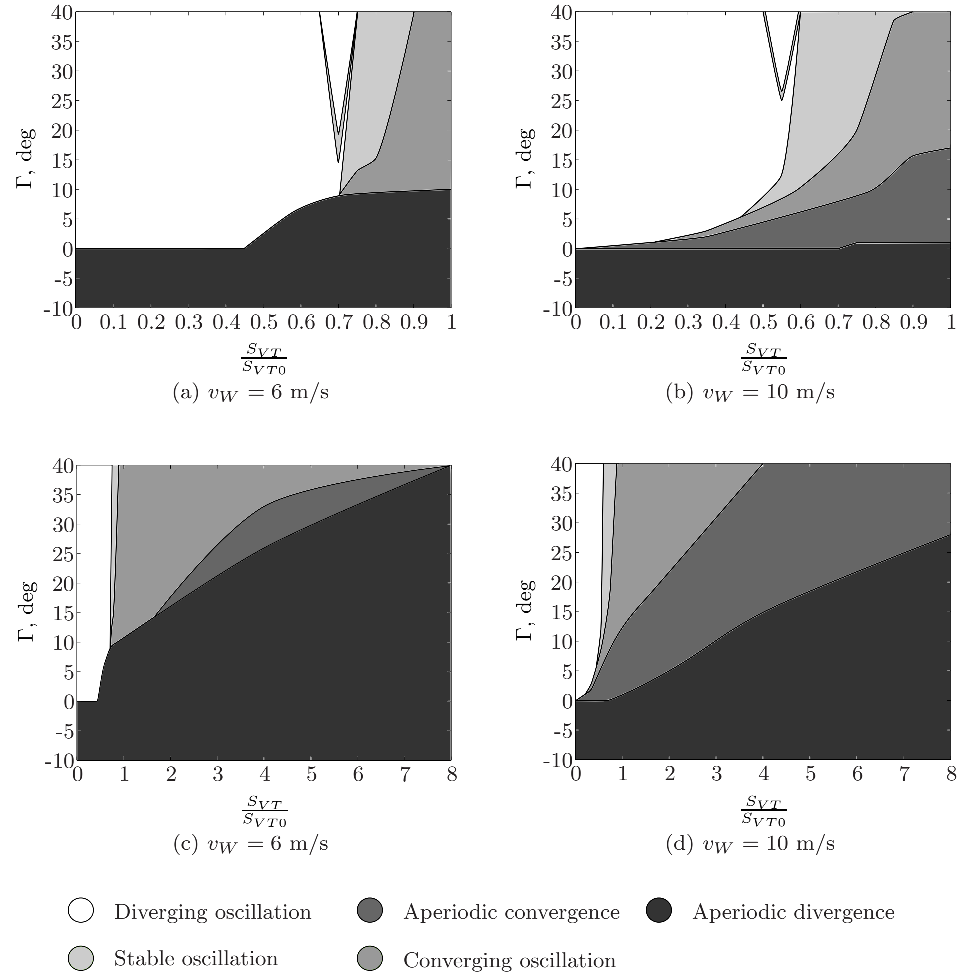

(a) $v_W = 6$ m/s

(b) $v_W = 10$ m/s

(c) $v_W = 6$ m/s

(d) $v_W = 10$ m/s

Fig. 20: Stability chart depending on $\frac{S_{VT}}{S_{VT0}}$ and Γ for two wind speeds.

At the boundary of diverging oscillation and stable oscillation something peculiar occurs, which is visible in Figs. 20a and 20b. At a vertical tail plane size slightly too small for stable oscillation, there seems to be a small band of Γ values that still yield a semi-stable oscillation. When the vertical tail plane area is reduced sightly from stable oscillation, the stable figure-eight pattern starts to oscillate itself. This behavior can be compared with the precession of the rotation axis of a spinning top. For most cases, the crossing of the figure-eight starts to move in Y^E direction, one circle becomes larger than the other and eventually the Kiteplane crashes into the ground.

Another feature that is invisible in Figs. 20c and 20d are the roots of the different stable domains. These figures reveal that there is always a converging oscillation domain below the stable oscillation domain, and that the arrangement of the aperiodic convergence domain is depending a lot on wind velocity.

The pendulum stability according to the five stability domains with a sample flight trajectory are displayed in Fig. 21. The equilibrium lines in Fig. 21 are calibrated to the average conditions during the trajectory.

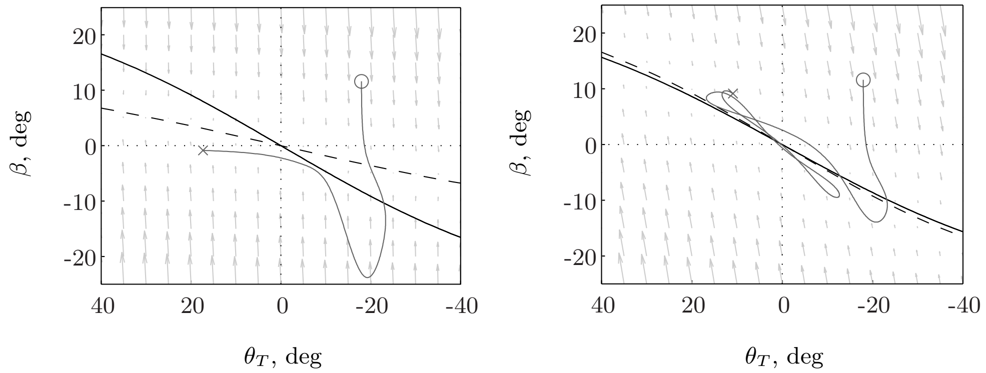

(a) Diverging oscillation (b) Stable oscillation

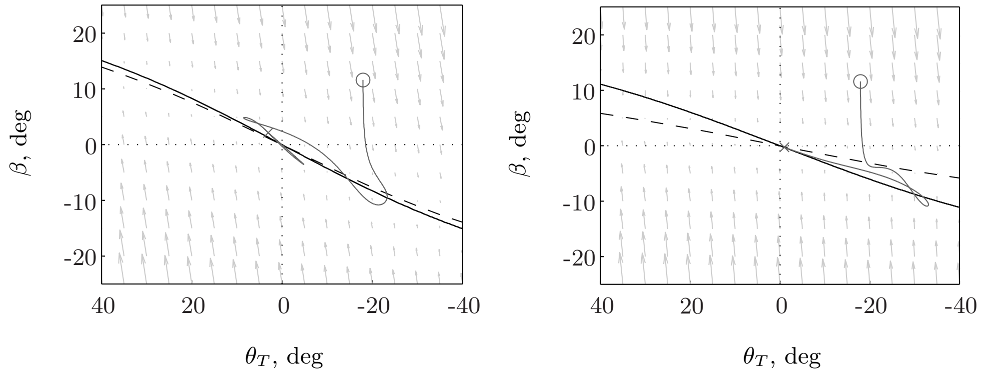

(c) Converging oscillation (d) Aperiodic convergence

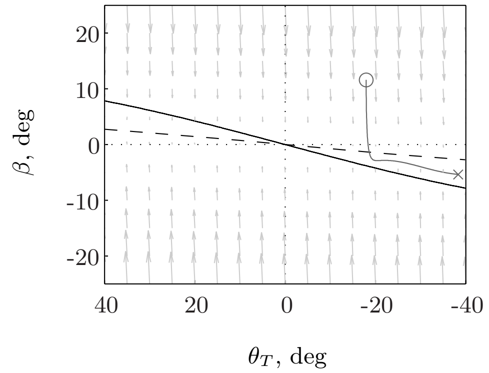

(e) Aperiodic divergence

Fig. 21: Pendulum stability with θ_T equilibrium — and β equilibrium $--$ according to the five different stability domains, including sample trajectories starting at the circle mark.

The first thing to notice is that the differences between the equilibrium lines is small compared to the resulting trajectory. While the behavior and geometry in both unstable domains is significantly different, the equilibrium lines have a similar slope difference. It appears that, in general, if the difference between the slope of the solid and dashed line becomes too large, the system becomes unstable.

The stable oscillation domain displayed in Fig. 21b is the desired stability space according to the pendulum stability analysis in Section III A. The dashed line is steeper than the solid line, which means that the Kiteplane converges to a sideslip angle that generates a resultant force toward $\theta_T = 0$. However, this configuration lacks damping configuration's lack of damping results in continued oscillations.

At the border of stable oscillation and converging oscillation, the dashed line is on top of the solid line. From the 2 DOF pendulum motion point of view, this is the border to unstable behavior. However, the longitudinal stability improves lateral stability and is in fact crucial in the entire converging domain.

If the solid line is only slightly steeper than the dashed line, the motion is still oscillatory. If the difference in slope becomes larger, the oscillations disappear. This is the domain of aperiodic convergence and illustrates the improved apparent lateral stability very clearly, because the acceleration arrows indicate divergence.

Nevertheless, if the lateral instability becomes too large for the longitudinal stabilization, the motion diverges as displayed in Fig. 21e. The absolute slope difference in Figs. 21d and 21e are about equal, but the relative difference is larger because the slopes in Fig. 21e are shallower.

As an additional illustration of the motion of the Kiteplane system, a sample trajectory of stable oscillation is displayed in Fig. 22. The trajectory starts with a launch from a slight asymmetric initial condition: $\chi = -10^\circ$ and $\psi = 10^\circ$.

Impact of operating conditions on stability. During kite flight, various operational conditions occur. Also, the presented model is a simplification of reality based on assumptions that have an impact on accuracy. For these reasons, it is important that stability holds for both varying conditions and small design variations. To determine the impact of these variations on stability

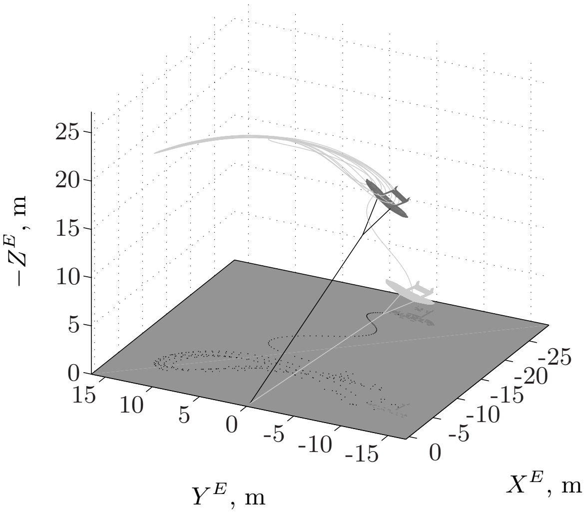

Fig. 22: Stable oscillation trajectory for $\Gamma = 20°$, $\frac{S_{VT}}{S_{VT0}} = 0.63$ and $v_W = 10\ \mathrm{ms}^{-1}$.

several simulations are run, where each simulation varies a single parameter. The results of these simulations are compared to the converging oscillation reference case with the following parameter values:

$$\begin{aligned} v_W &= 8 \ \text{m/s}, & \Gamma &= 20 \ \text{deg}, \\ l_T &= 25 \ \text{m}, & \frac{S_{VT}}{S_{VT0}} &= 1.5, \\ x_T &= 0.3 \ \text{m}. \end{aligned}$$

All other parameters are equal to the original design values. The simulation results are summarized in Table 2.

According to the results in Table 2, the stability of the reference case seems robust. To find out if the robustness holds for combined variations, the following two cases are assessed.

1. Inertia +30%, Γ +30% and $\frac{S_{VT}}{S_{VT0}}$ -30%
2. Inertia -30%, Γ -30% and $\frac{S_{VT}}{S_{VT0}}$ +30%

The first case, which leans toward diverging oscillations, as well as the second case, which leans toward aperiodic divergence, are in fact still converging. Although the latter is on the verge of aperiodic divergence, these results are promoting the idea of a configuration that is stable in the entire operating domain.

Table 2: Impact of operating conditions on stability.

Parameter variation		Asymmetric initial conditions	Lateral step gust of $0.5v_W$
Reference		Converging oscillation	Converging oscillation
Inertia	−30%	More damped oscillation	More damped oscillation
	+30%	Less damped oscillation	Less damped oscillation
Γ	−30%	Aperiodic convergence	Aperiodic convergence
	+30%	Less damped oscillation	Less damped oscillation
$\frac{S_{VT}}{S_{VT0}}$	−30%	Less damped oscillation	Less damped oscillation
	+30%	More damped oscillation	More damped oscillation
x_T	0.0 m	More damped oscillation	More damped oscillation[1]
	0.55 m	Aperiodic convergence	Aperiodic convergence
	0.6 m	Aperiodic divergence	Aperiodic divergence
l_T	10 m	More damped oscillation	More damped oscillation
	100 m	Equal damping, longer period	Equal damping, longer period and lower amplitude
v_W	4 ms^{-1}	Less damped oscillation[1]	Less damped oscillation[1]
	16 ms^{-1}	More damped oscillation[1]	More damped oscillation[1]

[1] Requires new trim setting for proper longitudinal equilibrium in α.

IV. Conclusions

The geometric requirements for stable flight dynamics of a Kiteplane are different from these of regular airplanes. Similarities are found in the longitudinal motion, but the constraints resulting from the tether and the bridle connection give rise to instabilities in the lateral motion outside the symmetry plane. The pendulum motion in particular poses additional requirements for stability.

With the developed rigid body model, an explanation is found for the pendulum instability of the Kiteplane design considered in the case study. The analytical analysis yields the hypothesis that a large wing dihedral angle combined with a small vertical tail plane area provides pendulum stability. The small vertical tail plane causes the equilibrium sideslip angle to be large enough for the effective lateral area to generate an aerodynamic force that opposes and overcomes the lateral component of gravity.

Numerical simulations of the derived equations of motion confirm the hypothesis, but the criteria on the geometry appear to be less strict. Due to the mixing of longitudinal and lateral motion, stability is achieved with a larger vertical tail plane area than predicted by the analytical results. In addition, it is found that reducing the horizontal tail plane area by 25 % improves the convergence of the longitudinal motion.

The numerical simulations are only partially successful in reconstructing the presented test flight, but this may be improved when more and accurate data becomes available for calibration of the model.

The results indicate that the stability of the Kiteplane is highly depending on lateral area parameters. More precisely, the simulation results show that the 2D Kiteplane design space spanned by dihedral angle and vertical tail plane area consists of the five different stability domains listed below.

- Unstable oscillation for a dihedral angle $> 5^\circ$ and a vertical tail $< 3\%$ wing area.
- Stable oscillation for a dihedral angle $\sim 25^\circ$ and a vertical tail $\sim 4.5\%$ wing area.
- Converging oscillation for a dihedral angle $\sim 25^\circ$ and a vertical tail $\sim 9\%$ wing area.
- Aperiodic convergence for a dihedral angle $\sim 25^\circ$ and a vertical tail $\sim 25\%$ wing area.
- Aperiodic divergence for a dihedral angle $< 10^\circ$ and a vertical tail $> 25\%$ wing area.

In respect to these stability domains, the investigated Kiteplane design features a too small lateral area that is distributed too far to the back. A geometry change that moves the design to the converging oscillation domain is, according to the simulation results, stable for a solid range in design inaccuracies and operational conditions.

ACKNOWLEDGMENTS

The authors are grateful for the financial support provided by the Rotterdam Climate Initiative and the province of Friesland. They appreciate the cooperation of Lam Sails Ltd. in the production and the engagement of R. Verheul of the ASSET Institute of Delft University of Technology in the design, construction and testing of the Kiteplane prototype.

REFERENCES

[1] Breukels, J. and Ockels, W. J., "Past, present and future of kites and energy generation," *Power and Energy Systems Conference 2007*, Clearwater, FL, USA, 3-5 Jan. 2007.

[2] Archer, C. and Caldeira, K., "Global Assessment of High-Altitude Wind Power," *Energies*, Vol. 2, No. 2, 2009, pp. 307-319.
doi: 10.3390/en20200307

[3] Rogner, H-H. et al., *World Energy Assessment: Energy and the challenge of sustainability*, Chapter 5: Energy Resources, United Nations Development Programme, New York, NY, USA, 2000.

[4] Loyd, L., "Crosswind Kite Power," *Journal of Energy*, Vol. 4, No. 3, 1980.
doi: 10.2514/3.48021

[5] Ockels, W. J., "Wind energy converter using kites," European Patent EP084480, Dutch Patent NL1004508, Spanish Patent SP2175268, US Patent US6072245, filed Nov. 1996.

[6] Ockels, W. J., "Laddermill, a novel concept to exploit the energy in the airspace," *Journal of Aircraft Design*, Vol. 4, 2001, pp. 81-97.
doi: 10.1016/S1369-8869(01)00002-7

[7] Harvey, M., "The quest to find alternative sources of renewable energy is taking to the skies," *Times Online*, URL: `http://business.timesonline.co.uk/` [cited 19 May 2010].

[8] "KitVes Project Funding," URL: `http://www.kitves.com/funding.aspx` [cited 19 May 2010].

[9] Botter, M., "Rotterdam ondersteunt Ockels' project 'Laddermillship' met €1 miljoen," URL: `http://www.obr.rotterdam.nl/smartsite2138537.dws` [cited 19 May 2010].

[10] Vance, E., "Wind power: High hopes," *Nature*, Vol. 460, 2009, pp. 564-566.
doi: 10.1038/460564a

[11] Canale, M., Fagiano, L., and Milanese, M., "KiteGen: A revolution in wind energy generation," *Energy*, Vol. 34, 2009, pp. 355-361.
doi: 10.1016/j.energy.2008.10.003

[12] Lansdorp, B. and Ockels, W. J., "Comparison of concepts for high-altitude wind energy generation with ground based generator," *2nd China International Renewable Energy Equipment & Technology Exhibition and Conference*, Beijing, China, 25-27 May 2005.

[13] Lansdorp, B. and Ockels, W. J., "Design of a 100 MW laddermill for wind energy generation from 5 km altitude," *7th World Congress on Recovery, Recycling and Reintegration*, Beijing, China, 25-29 Sept. 2005.

[14] Bryant, L. W., Brown, W. S., and Sweeting, N. E., "Collected Researches on the Stability of Kites and

Towed Gliders," Tech. Rep. 2303, Ministry of Supply, Aeronautical Research Council, London, UK, 1942.

[15] Etkin, B., "Stability of a Towed Body," *Journal of Aircraft*, Vol. 35, No. 2, 1998, pp. 197-205.
doi: 10.2514/2.2308

[16] Lambert, C. and Nahon, M., "Stability Analysis of a Tethered Aerostat," *Journal of Aircraft*, Vol. 40, No. 4, 2003, pp. 705-715.
doi: 10.2514/2.3149

[17] Breukels, J., "KitEye," Faculty of Aerospace Engineering, Delft University of Technology, Delft, The Netherlands, 2005.

[18] Breukels, J. and Ockels, W. J., "Design of a Large Inflatable Kiteplane," No. AIAA 2007-2246, *48th AIAA/ASME/ASCE/AHS/AHC Structures, Structural Dynamics, and Materials Conference*, Honolulu, HI, USA, April 2007.

[19] Breukels, J. and Ockels, W. J., "Tethered "kiteplane" design for the Laddermill project," *4th World Wind Energy Conference & Renewable Energy Exhibition 2005*, Melbourne, Australia, 2-5 Nov. 2005.

[20] Williams, P., Lansdorp, B., Ruiterkamp, R., and Ockels, W. J., "Modeling, Simulation, and Testing of Surf Kites for Power Generation," No. AIAA 2008-6693, *AIAA Modeling and Simulation Technologies Conference and Exhibit*, Honolulu, Hi, USA, 18-21 Aug. 2008.

[21] Williams, P., Lansdorp, B., and Ockels, W. J., "Optimal Crosswind Towing and Power Generation with Tethered Kites," *AIAA Journal of Guidance, Control and Dynamics*, Vol. 31, No. 1, 2008, pp. 81-93.
doi: 10.2514/1.30089

[22] Fagiano, L., *Control of Tethered Airfoils for High-Altitude Wind Energy Generation*, Ph.D. Dissertation, Royal Turin Polytechnic, Turin, Italy, 2009.

[23] Houska, B. and Diehl, M., "Optimal Control of Towing Kites," No. ThA10.3, *Proceedings of the 45th IEEE Conference on Decision & Control*, San Diego, CA, USA, 13-15 Dec. 2006.

[24] Dadd, G. M., Hudson, D. A., and Shenoi, R. A., "Comparison of Two Kite Force Models with Experiment," *Journal of Aircraft*, Vol. 47, No. 1, 2010, pp. 212-224.
doi: 10.2514/1.44738

[25] Meijaard, J. P., Ockels, W. J., and Schwab, A. L., "Modelling of the Dynamic Behaviour of a Laddermill, A Novel Concept to Exploit Wind Energy," *Proceedings of the 3rd International Symposium on Cable Dynamics*, Trondheim, Norway, 16-18 Aug. 1999, pp. 229-234.

[26] Zatzkis, H., *Fundamental formulas of physics*, Vol. 1, Section 1.4, Courier Dover, 2nd ed., 1960.

[27] Williams, P., Lansdorp, B., and Ockels, W. J., "Optimal Trajectories for Tethered Kite Mounted

on a Vertical Axis Generator," No. AIAA 2007-6706, *AIAA Modeling and Simulation Technologies Conference and Exhibit*, Hilton Head, SC, USA, 20-23 Aug. 2007.

[28] Williams, P., Lansdorp, B., and Ockels, W. J., "Modeling of Optimal Power Generation using Multiple Kites," No. AIAA 2008-6691, *AIAA Modeling and Simulation Technologies Conference and Exhibit*, Honolulu, HI, 18-21 Aug. 2008.

[29] Williams, P., Lansdorp, B., and Ockels, W. J., "Flexible Tethered Kite with Moveable Attachment Points, Part I: Dynamics and Control," No. AIAA 2007-6628, *AIAA Atmospheric Flight Mechanics Conference and Exhibit*, Hilton Head, SC, USA, 20-23 Aug. 2007.

[30] Fink, M. P., "Full-Scale investigation of the aerodynamic characteristics of a sailwing of aspect ratio 5.9," Tech. Rep. NASA TN D-5047, Langley Research Center, National Aeronautics and Space Administration, Langley Station, Hampton, VA, USA, 1969.

[31] Hoerner, S. F., *Fluid-Dynamic Drag*, Hoerner Fluid Dynamics, Vancouver, Canada, 1965.

[32] Hoak, D. E. and Finck, R. D., "The USAF Stability and Control DATCOM," Tech. Rep. TR-83-3048, Section 4.4.1, Air Force Wright Aeronautical Laboratories, Wright-Patterson Air Force Base, Fairborn, OH, USA, 1960.

[33] Torenbeek, E., *Synthesis of Subsonic Airplane Design*, Appendix A-3.3, Delft University Press, Delft, The Netherlands, 1982.

[34] Etkin, B., *Dynamics of Atmospheric Flight*, John Wiley & Sons, Inc, New York, NY, USA, 1972.

[35] Roskam, J., *Airplane Flight Dynamics and Automatic Flight Controls*, DARcorporation, Lawrence, KS, USA, 2001.

[36] Mulder, J. A., van Staveren, W. H. J. J., van der Vaart, J. C., and de Weerdt, E., *Flight Dynamics*, Delft University of Technology, Delft, The Netherlands, 2006.